On the Connection Between Near and Far Pressure Fields of a Turbulent Jet

Dimitri Papamoschou*
University of California, Irvine, Irvine, CA, 92697, USA

The paper presents the development of a simple stochastic model for the noise source of a round turbulent jet. The model is defined on a surface at the rotational/irrotational boundary of the jet and comprises a linear pressure event with random origin and random helical mode. The probability density function for the event's axial origin is derived from the statistics of coherent structures in shear layers. The distribution for the helical mode is mostly empirical and driven by the need to match the polar directivity of sound emission in the far field. The generic form of the event is a self-similar wavepacket whose shape parameters are determined by least-squares matching of the far-field sound pressure level at a wide range of frequencies and polar angles. Initial results indicate that the model reproduces, in a qualitative sense, key statistics of the jet acoustic field, including the near-field space-time correlation, the broadening of the far-field spectral density with increasing polar angle from the jet axis, and the coherence between the near and far fields. For the latter, the analysis indicates that the rapid decline in the coherence with increasing polar angle is primarily due to the randomness of the event's axial origin.

I. Introduction

The aerospace community needs design tools that can predict aircraft engine noise with high fidelity and rapid turnaround times. Prediction of jet turbulent mixing noise and its interaction with airframe surfaces constitutes an immense theoretical and computational challenge. The noise source is stochastic and highly sensitive on the instantaneous and time-averaged features of the jet flow. Common scattering techniques are designed for deterministic, not random fields. A solution from first principles, while possible in principle, would require inordinate computational resources for a single solution, thus cannot be considered a practical predictive tool. We seek simplification of the jet noise source that retains the basic physics and has the potential to yield high-fidelity predictions of the radiated sound and its scattering around objects at relatively low computational cost.

In the approach developed here the jet noise source is prescribed as linear partial fields on a conical-shaped "radiator surface" at the boundary between the inner nonlinear rotational flow field and outer linear pressure field. It is on this surface that the pressure distribution reflects the "footprint" of the turbulent eddies, as shown by previous studies.[1–3] If the boundary is taken to be at some distance from the edge of the jet, the hydrodynamic information is lost and all that remains is the acoustic field. Once the noise source on the radiator surface is properly modeled, propagation to an observer outside the surface involves well established linear tools such as the boundary element method.

In this paper we discuss fundamental statistics of the coherent structures that constitute the main noise source, then construct an elemental model for the jet noise source that is based on those statistics. A specific shape for the model is then assumed that is based on the wavepacket anzatz, a concept that has received considerable study.[4–9] The proposed model is essentially a stochastic extension of the wavepacket model proposed by Papamoschou.[10] The ability of the model to reproduce key experimental trends of the near and far acoustic fields is examined. In addition to its potential practical usefulness, the analysis also helps shed some light on a major unresolved issue in jet aeroacoustics, the lack of near-far correlation at large angles to the jet axis.[11,12]

*Professor, Department of Mechanical and Aerospace Engineering, Fellow AIAA

II. Development of Key Distributions

A. Coherent Structures in Shear Layers

The pioneering experiments of Brown and Roshko[13] established the prominent role of coherent turbulent structures in shear-layer mixing. The coherent structures are of integral length scale, thus defining the extent of the mixing region, and travel downstream with a fairly constant convective velocity U_c. Because the structures grow with downstream distance, they merge with each other - a phenomenon often referred to as vortex pairing.[13] The merger process imparts a lifetime to each vortex. At a given axial station x_0, the spacing between eddies ℓ, which we can interpret as a wavelength, is not fixed but is random. See Fig. 1. Analysis by Bernal[14] showed that the distribution of the wavelength is lognormal. Defining $\xi = \ell/x_0$, where x_0 is the axial coordinate, the probability density function (PDF) for ξ has the form

$$f_\xi(\xi) \;=\; \frac{1}{\xi\sigma\sqrt{2\pi}}\exp\left\{-\frac{1}{2\sigma^2}\left[\ln\left(\frac{\xi}{\mu}\right)+\frac{\sigma^2}{2}\right]^2\right\} \tag{1}$$

where μ is the expected value and σ^2 is the variance of ξ. Conversely, the probability that a wavelength ℓ occurs in the interval $[x_0, x_0 + dx_0]$ is also lognormal.[14] The PDF of $\zeta = x_0/\ell$ is

$$f_\zeta(\zeta) \;=\; \frac{1}{\zeta\sigma\sqrt{2\pi}}\exp\left\{-\frac{1}{2\sigma^2}\left[\ln\left(\frac{\zeta}{\mu}\right)+\frac{\sigma^2}{2}\right]^2\right\} \tag{2}$$

where μ is the expected value and σ^2 is the variance of ζ. In Eq. 1, x_0 is fixed (deterministic) and ℓ is random. The roles are reversed in Eq. 2, where we seek the distribution of x_0 for a fixed wavelength.

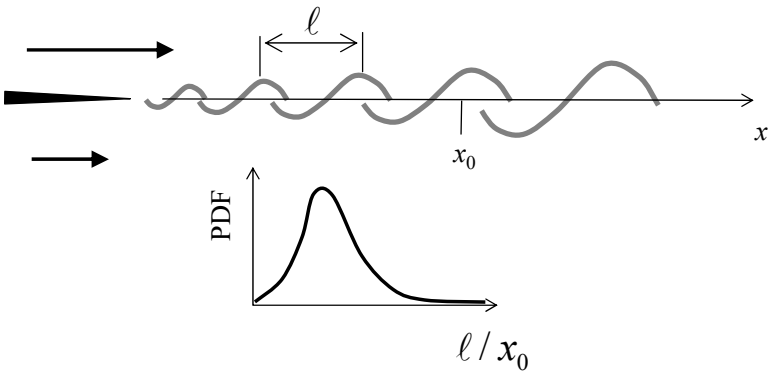

Figure 1. Eddy spacing in a turbulent shear layer. Based on Ref. 14.

B. Distribution of Event Origin

For the turbulent jet, it is reasonable to assume that the basic statistics discussed above hold in the shear layer region surrounding the potential core,[15] although here we will also include the region past the potential core. We seek the description of a noise generating event at fixed frequency ω. The event will be "centered" at an axial station x_0 that is random. This location can also be interpreted as the origin of the event. We seek the distribution of x_0 for fixed frequency ω, and denote this PDF as $f_{x_0}(x_0, \omega)$. The frequency is connected to the wavelength via the convective velocity:

$$\omega \;=\; 2\pi\frac{U_c}{\ell} \tag{3}$$

If the convective velocity U_c were constant, the relation between the f_{x_0} and f_ζ would be straightforward. However, in a jet flow U_c is constant only within the potential core region and declines downstream as the mean velocity decays with axial distance. Therefore, $U_c = U_c(x_0)$. The derivation of f_{x_0} is thus more involved. First, we write

$$x_0 \;=\; \frac{x_0}{\ell}\ell \;=\; \frac{\zeta}{\omega}2\pi U_c(x_0) \tag{4}$$

where we used Eq. 3 in the last step. Denoting the solution to Eq. 4 as

$$x_0 \;=\; G\left(\frac{\zeta}{\omega}\right) \tag{5}$$

it is clear from Eq. 4 that it has a root at

$$\left(\frac{\zeta}{\omega}\right)_{\text{root}} \;=\; \frac{x_0}{2\pi U_c(x_0)} \tag{6}$$

Following the relations in Papoulis,[16] the PDF of x_0 is given by

$$f_{x_0}(x_0,\omega) \;=\; \frac{1}{\left|G'\left[\left(\frac{\zeta}{\omega}\right)_{\text{root}}\right]\right|} f_{\zeta/\omega}\left[\left(\frac{\zeta}{\omega}\right)_{\text{root}}\right] \;=\; \frac{1}{G'\left[\dfrac{x_0}{2\pi U_c(x_0)}\right]} f_{\zeta/\omega}\left[\frac{x_0}{2\pi U_c(x_0)}\right] \tag{7}$$

The PDF of ζ/ω is readily connected to the PDF of ζ according to

$$f_{\zeta/\omega}\left(\frac{\zeta}{\omega}\right) \;=\; |\omega| f_\zeta(\zeta) \;=\; \omega f_\zeta\left(\frac{\omega x_0}{2\pi U_c(x_0)}\right) \tag{8}$$

yielding

$$f_{x_0}(x_0,\omega) \;=\; \frac{\omega}{G'\left[\dfrac{x_0}{2\pi U_c(x_0)}\right]} f_\zeta\left(\frac{\omega x_0}{2\pi U_c(x_0)}\right) \tag{9}$$

In the above derivations we use the fact that G' is always positive and constrain our analysis to $\omega \geq 0$.

For a single-stream round jet with exit velocity U_j and nozzle diameter D_j, the following function provides an approximation of the axial evolution of the centerline mean velocity $u_m(x)$:

$$\frac{u_m(x)}{U_j} \;=\; \frac{\alpha^{-1/\beta}}{\dfrac{x}{D_j}} \left\{\tanh\left[\alpha\left(\frac{x}{D_j}\right)^{\beta}\right]\right\}^{1/\beta} \tag{10}$$

The values $\alpha = 2.8$ and $\beta = 0.016$ provide an excellent representation of the axial velocity profile of a cold Mach 0.9 air jet,[17] as shown in Fig. 2. The convective velocity is taken to be a constant fraction of the mean centerline velocity:

$$U_c(x_0) \;=\; \frac{U_c(0)}{U_j} u_m(x_0) \tag{11}$$

where $U_c(0)/U_j$ will be one of the parameters that define the event. The convective Mach number then is

$$M_c(x_0) \;=\; \frac{U_c(x_0)}{a} \;=\; \frac{U_c(0)}{U_j}\;\frac{u_m(x_0)}{a} \tag{12}$$

where a is the ambient speed of sound.

For several of the results to be presented in this paper, the frequency will take the non-dimensional form of Strouhal number

$$Sr \;=\; \frac{\omega D_j}{2\pi U_j} \tag{13}$$

Figure 3 illustrates the behavior of f_{x_0} in the Mach 0.9 jet, with $U_c(0)/U_j = 0.62$, $\mu = 3.4$, and $\sigma = 0.90$.

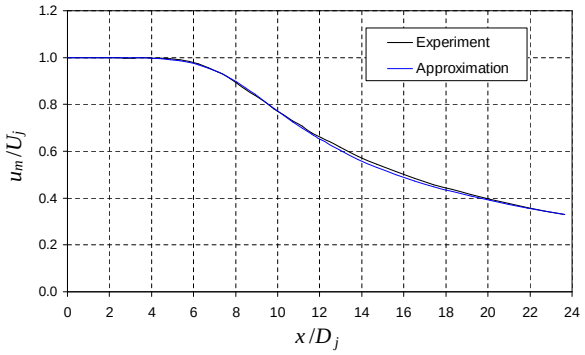

Figure 2. Axial distribution of mean centerline velocity for cold Mach 0.9 jet.

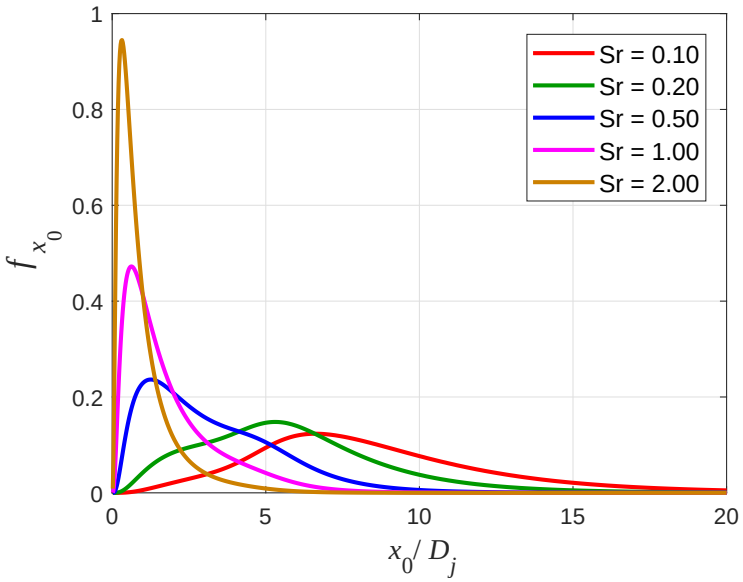

Figure 3. Illustration of the PDF of x_0 at different Strouhal numbers

C. Distribution of Azimuthal Mode

Considering application to a round turbulent jet, the event will be assumed to be fully coherent azimuthally with helical mode n. This is a simplification as it is known that the azimuthal coherence in a turbulent jet is a decreasing function of frequency, and the azimuthal correlation scale reaches very small values at Strouhal numbers above unity.[18] The helical mode n will be treated as a random variable with discrete PDF $f_n(\omega)$. The distribution of the helical mode will be an important component in the modeling. According to the guidance of Ref. 10, the helical content must increase with increasing frequency for the modeled emission to match the polar directivity of the far-field sound. In that work, only one helical mode was present at a given frequency. In reality, a number of helical modes may coexist, especially at high frequency.[19] Here we assume a distribution of helical modes, using the model

$$f_n(\omega) = \frac{1}{\sum_{k=-K}^{K}[\beta(\omega)]^{k^2}} \sum_{k=-K}^{K} [\beta(\omega)]^{k^2} \delta_{n,n_\omega-k} \tag{14}$$

where K denotes the number of modes on either side of the dominant mode n_ω, $\beta(\omega) < 1$ is an adjustable function, $\delta_{i,j}$ is the Kronecker delta, and the normalization (summation in the denominator) satisfies the

requirement

$$\sum_{n=-\infty}^{\infty} f_n(\omega) = 1 \tag{15}$$

At fixed frequency ω, Eq. 14 results in a Gaussian distribution of $f_n(\omega)$, as exemplified in Fig. 4. The width of the distribution is controlled by $\beta(\omega)$, which will be selected as an increasing function of ω. This reflects the dominance of only a few modes at low frequency, and the expectation of a rich helical content at high frequency. It is easy to see that Eq. 14 can be generalized for different powers of k (e.g., selecting β^k would result in an exponential distribution), although here we consider only the Gaussian model.

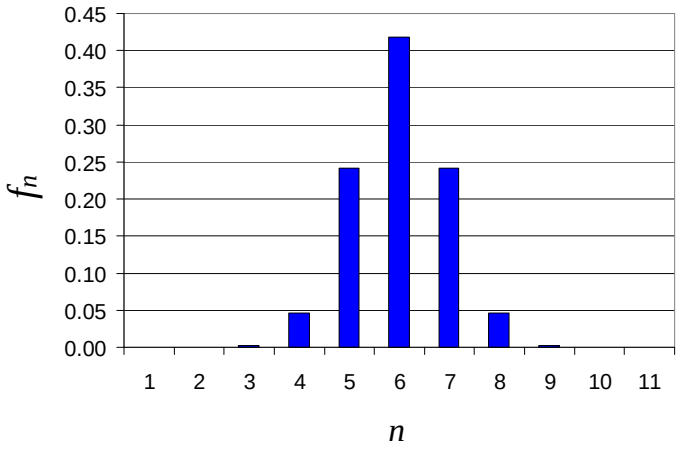

Figure 4. Illustration of the PDF of helical mode n at Strouhal number $Sr = 3$. Here the dominant mode is $n_\omega = 6$.

The following are preliminary, empirical formulas for n_ω and β that have resulted from the optimization process discussed in Section V.A. They are illustrative of main trends and are subject to refinement as the fidelity of the model improves.

$$\begin{aligned} n_\omega &= \begin{cases} 0 \ , & Sr \le 0.22 \\ \lfloor 4.1(Sr - 0.22)^{0.66} \rfloor \ , & Sr > 0.22 \end{cases} \\ \beta &= 0.85 \ \tanh[0.07(Sr)^{2.6}] \end{aligned} \tag{16}$$

where $\lfloor \ \rfloor$ denotes the floor function. Equation 16 says that the dominant helical mode n_ω is zero at low Strouhal number, then rises with increasing Strouhal number following approximately the trend found in Ref. 10; and that the width the the Gaussian distribution of f_n increases with Strouhal number.

III. Surface Source Model - General Treatment

Consider a round turbulent jet and an axisymmetric surface located at the boundary between the non-linear rotational flow and the linear pressure field, as depicted in Fig. 5. For brevity we will refer to this surface as the radiator surface. It is surmised that random events on this surface, which define the noise source, have statistics similar to those of the coherent structures in the jet flow. The pressure field on the surface will be denoted by p, and the far-field pressure will be denoted by P.

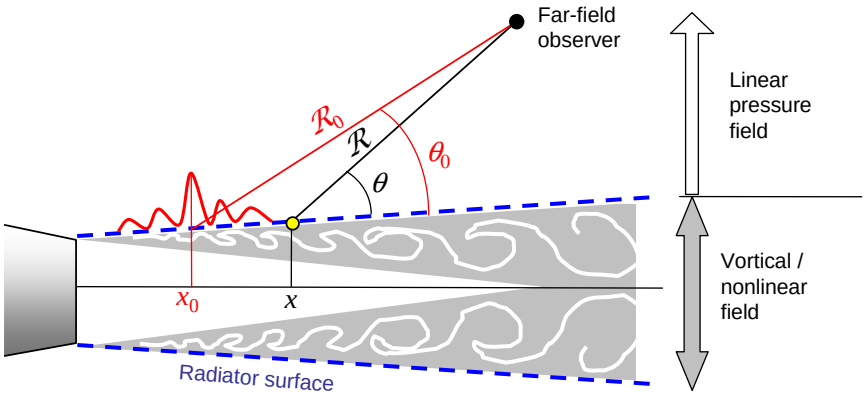

Figure 5. Generalized surface source model.

A. Surface Event

On the radiator surface, at fixed frequency ω, we consider a random event of the form

$$p(x,\phi,t) \;=\; \epsilon(\omega)\; q(x,x_0,\omega)\; e^{in(\phi-\phi_0)}e^{-i\omega t} \tag{17}$$

Here ϵ is the amplitude; x and ϕ are fixed axial and azimuthal coordinates (probe location); x_0 and ϕ_0 signify the axial and azimuthal origins of the event; n is the helical mode; and q is a function with finite axial extent X. In the formulation of the event, ϵ, x_0, ϕ_0, and n are independent random variables. The PDFs for x_0 and n were discussed in Section II. Considering that the jet is axisymmetric and unforced, the PDF for ϕ_0 is uniform at $1/(2\pi)$.

B. Far Field Pressure

A far-field observer is located at distance $\mathcal{R} >> X$ and polar angle θ relative to the probe position x and the local inclination of the radiator surface (Fig. 5). With reference to the event origin x_0, the observer is located at distance $\mathcal{R}_0$ and polar angle θ_0 . Note that $\mathcal{R}_0$ and θ_0 are random variables. The sound measured by the far-field observer from this particular event has the form

$$P(x_0,\mathcal{R}_0,\theta_0,\phi,t) \;=\; \epsilon(\omega)\; Q_n(x_0,\theta_0,\omega)\; \frac{e^{i\frac{\omega}{a}\mathcal{R}_0}}{4\pi\mathcal{R}_0}\; e^{in(\phi-\phi_0)}e^{-i\omega t} \tag{18}$$

Q_n is a deterministic function that depends on the specific form of q, the shape of the radiator surface, and the helical mode n. We recognize the third term on the right-hand-side of Eq. 18 as the 3D free-space Green's function, representing the spherical spreading in the far field of a localized disturbance. Equation 18 gives the far-field pressure in terms of the event coordinates. To convert to the probe coordinates, we note that $\theta \approx \theta_0$ and

$$\mathcal{R}_0 \;\approx\; \mathcal{R} + (x - x_0)\cos\theta \tag{19}$$

where we assumed that the slope of the radiator surface is very small. Even though the difference between $\mathcal{R}_0$ and $\mathcal{R}$ is insignificant for the denominator of the Green's function, it is extremely important for the exponent of the numerator. Using the probe coordinates, we write

$$P(x_0,\mathcal{R},\theta,\phi,t) \;=\; \frac{\epsilon(\omega)}{4\pi\mathcal{R}}\; Q_n(x_0,\theta,\omega)\; e^{in(\phi-\phi_0)}\; e^{-i\omega(t-\mathcal{R}/a)}e^{i\frac{\omega}{a}(x-x_0)\cos\theta} \tag{20}$$

C. Statistics

Statistics at a fixed frequency ω are obtained by integrating or summing the relevant quantities over all possible outcomes. Then, integration over frequency gives the overall correlations. The operation <> will denote the expected value (ensemble average) and $(\;)^*$ will mean the complex conjugate. First we discuss general procedures that will be employed in the calculation of statistics, then proceed with deriving the statistics of interest.

1. General Procedures

In the following we will develop expressions for correlations of the type $< pp^* >$ (near field), $< PP^* >$ (far field) and $< pP^* >$ (near to far field). The amplitude ϵ being an independent random variable that appears in both p and P, all the aforementioned correlations will end up with the factor $< \epsilon\epsilon^* >$, which for convenience we denote

$$E(\omega) \ = < \epsilon \ \epsilon^* > \tag{21}$$

The azimuthal term $e^{in(\phi-\phi_0)}$ will appear in both p and P, therefore will drop out of all the correlations. Since the PDF for ϕ_0 is assumed uniform at $1/(2\pi)$, integration over $[0, 2\pi]$ gives unity. The treatment of the helical modes will involve summations of the type

$$\sum_{n=-\infty}^{\infty} f_n(\omega)[\ldots]$$

where $f_n(\omega)$ is the (discrete) PDF for n. If the term in the brackets does not depend on n, then it is simply multiplied by unity as we must satisfy $\sum_{-\infty}^{\infty} f_n(\omega) = 1$. Finally, the treatment of the random origin x_0 will involve integrals of the type $\int_0^{\infty}[\ldots]f_{x_0}dx_0$.

In the analysis that follows, quantities in the frequency domain will be denoted by the subscript ω. Axisymmetry will be assumed, so the statistics at the same azimuthal angle will be independent of the azimuthal angle. Only the important arguments will be included to reduce clutter.

2. Axial Space-Time Correlation on Surface

The axial space-time correlation of the surface pressure at given frequency is defined by

$$R_{pp,\omega}(x;\xi,\tau) \ = < p(x,\phi,t)p^*(x+\xi,\phi,t+\tau) > \tag{22}$$

Inserting Eq. 17,

$$R_{pp,\omega}(x;\xi,\tau) \ = \ E(\omega)\int_0^{\infty} q(x,x_0,\omega)q^*(x+\xi,x_0,\omega)e^{i\omega\tau} \ f_{x_0}(x_0,\omega) \ dx_0 \tag{23}$$

The overall space-time correlation is obtained by integrating over all frequencies:

$$R_{pp}(x;\xi,\tau) \ = \frac{1}{2\pi}\int_0^{\infty}\int_0^{\infty} \ E(\omega)q(x,x_0,\omega)q^*(x+\xi,x_0,\omega)e^{i\omega\tau} \ f_{x_0}(x_0,\omega) \ dx_0 d\omega \tag{24}$$

Equation 24 follows the well-known relation between cross-correlation and cross-spectral density,[16] with the constraint that negative frequencies (negative wavelengths) are not physically meaningful for the problem addressed here; therefore, the integration is restricted to positive frequencies. The same argument holds for the subsequent integrations over frequency reported here.

3. Variance on Surface

The variance at fixed frequency (autospectral density) is obtained from the space-time correlation with $\xi = 0$ and $\tau = 0$. From Eq. 23,

$$R_{pp,\omega}(x;0,0) \ = \ E(\omega)\int_0^{\infty} |q(x,x_0,\omega)|^2 \ f_{x_0}(x_0,\omega) \ dx_0 \tag{25}$$

The overall variance is similarly obtained from Eq. 24,

$$R_{pp}(x;0,0) \ = \ \frac{1}{2\pi}\int_0^{\infty}\int_0^{\infty} \ E(\omega)|q(x,x_0,\omega)|^2 \ f_{x_0}(x_0,\omega) \ dx_0 d\omega \tag{26}$$

4. Far-Field Autospectral Density

The autospectral density of the far-field pressure is

$$R_{PP,\omega}(\mathcal{R},\theta) \;=< PP^* > \tag{27}$$

Using Eq. 20,

$$R_{PP,\omega}(\mathcal{R},\theta) \;= \frac{E(\omega)}{16\pi^2\mathcal{R}^2} \sum_{n=-\infty}^{\infty} f_n(\omega) \int_0^{\infty} \mid Q_n(x_0,\theta,\omega)\mid^2 f_{x_0}(x_0,\omega)\; dx_0 \tag{28}$$

The variance of the far-field pressure is obtained from

$$R_{PP}(\mathcal{R},\theta) \;=\; \frac{1}{2\pi}\int_0^{\infty} R_{PP,\omega}(\mathcal{R},\theta) d\omega \tag{29}$$

5. Surface to Far-Field Correlation

We are interested in the correlation between the probe signal and the far-field pressure at the same azimuthal angle:

$$R_{pP,\omega}(x,\theta;\tau) \;=< p(x,t)P^*(x_0,\mathcal{R},\theta,t+\tau) > \tag{30}$$

Using Eqs. 17 and 20,

$$R_{pP,\omega}(x,\theta;\tau) = \frac{E(\omega)}{4\pi\mathcal{R}} e^{i\omega(\tau-\mathcal{R}/a)} \sum_{n=-\infty}^{\infty} f_n(\omega) \int_0^{\infty} Q_n^*(x_0,\theta,\omega)\; q(x,x_0,\omega)\; e^{-i\frac{\omega}{a}(x-x_0)\cos\theta} f_{x_0}(x_0,\omega)\; dx_0 \tag{31}$$

The overall correlation at the retarded time $\tau \;=\; \mathcal{R}/a$ is obtained from

$$R_{pP}(x,\theta) \;=\; \frac{1}{2\pi}\int_0^{\infty} R_{pP,\omega}(x,\theta;\mathcal{R}/a) d\omega \tag{32}$$

IV. Surface Source Model - Wavepacket Event

We specify the relations developed in Section II to a class of waveforms that simulate salient features of instability waves.[5,7,9,10,20,21] The waveform at a particular frequency ω will be prescribed on a cylindrical surface of radius $r(x_0)$, where r typically grows linearly with x_0. Thus the totality of events at all frequencies falls on a conical surface, but each individual event is defined on a local cylinder. This simplifies significantly the analysis compared to a conical treatment.[5] Figure 6 presents this concept.

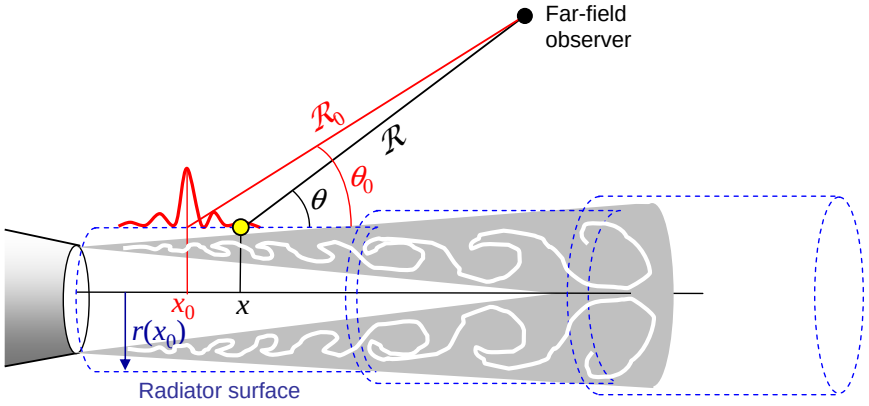

Figure 6. Wavepacket surface source model.

A. Surface Event

In Eq. 17, the function $q(x, x_0, \omega)$ assumes the form

$$q(x, x_0, \omega) \;=\; W\left[\frac{\omega}{U_c(x_0)}(x - x_0)\right] \exp\left[i\frac{\omega}{U_c(x_0)}(x - x_0)\right] \tag{33}$$

which describes a "self-similar" wavepacket[10] whose growth-decay envelope W scales with ω. The ratio ω/U_c is the instability wavenumber and $U_c(x_0)$ is the convective velocity of the instability wave. The origin of the wavepacket is at x_0.

B. Far Field Pressure

Following the analysis of Ref. 10, the far-field pressure of the wavepacket event is given by Eq. 20 with

$$Q_n(x_0, \theta_0, \omega) \;=\; 4\frac{U_c(x_0)}{i\omega}\,\frac{\widehat{W}\left[M_c(x_0)\cos\theta - 1\right]}{H_n^{(1)}\left[\frac{\omega}{a}r(x_0)\sin\theta\right]} \tag{34}$$

where

$$\widehat{W}(\eta) \;=\; \int_{-\infty}^{\infty} W(x)e^{-i\eta x}dx$$

is the Fourier transform of W and $H_n^{(1)}$ is the Hankel function of the first kind of order n.

C. Statistics

The statistics for the wavepacket pressure field are obtained by inserting in Eqs. 23-32 the specific forms for $q(x, x_0, t)$ and $Q_n(x_0, \theta_0, \omega)$ given above. Here we highlight two metrics of interest. For brevity we omit the radial distance $\mathcal{R}$ from the arguments.

1. Far Field Autospectral Density

Combining Eqs. 28 and 34,

$$R_{PP,\omega}(\theta) \;=\; \frac{E(\omega)}{\pi^2\mathcal{R}^2\omega^2}\sum_{n=-\infty}^{\infty} f_n(\omega)\int_0^{\infty} U_c^2(x_0)\left|\frac{\widehat{W}\left[M_c(x_0)\cos\theta - 1\right]}{H_n^{(1)}\left[\frac{\omega}{a}r(x_0)\sin\theta\right]}\right|^2 f_{x_0}(x_0, \omega)\; dx_0 \tag{35}$$

The magnitude of $\widehat{W}$ is maximized when its argument is at or near zero. For $M_c \geq 1$, this occurs at $\cos\theta = 1/M_c$. For $M_c < 1$ the amplitude of $\widehat{W}$ does not have a maximum with polar angle and increases monotonically as $\theta \to 0$. The strongest contribution in the integral of Eq. 35 comes from the potential core region where U_c has its maximum (constant) value. The integrand declines rapidly as x_0 increases past the end of the potential core. For a supersonic jet, the angle of peak emission reflects the aggregate contribution of the events represented by the integration, but will be close to the value based on M_c within the potential core.

2. Surface to Far-Field Correlation

We insert Eqs. 33 and 34 in Eq. 31, and evaluate at the retarded time $\tau = \mathcal{R}/a$. There are two exponentials that involve $x - x_0$, one arising from the Green's function (Eq. 31) and the other from the wavepacket formulation (Eq. 33). Combining these exponentials we obtain

$$\begin{aligned} R_{pP,\omega}(x, \theta; \tau = \mathcal{R}/a) \;=\; & \frac{iE(\omega)}{\pi\mathcal{R}\omega}\sum_{n=-\infty}^{\infty} f_n(\omega)\int_0^{\infty} U_c(x_0)\,\frac{\widehat{W}^*\left[M_c(x_0)\cos\theta - 1\right]}{H_n^{(2)}\left[\frac{\omega}{a}r(x_0)\sin\theta\right]} \\ & \times W\left[\frac{\omega}{U_c(x_0)}(x - x_0)\right]\exp\left\{i\frac{\omega}{a}\left[\frac{1}{M_c(x_0)} - \cos\theta\right](x - x_0)\right\}\; f_{x_0}(x_0, \omega)\; dx_0 \end{aligned} \tag{36}$$

Equation 36 provides insight into the correlation between the near and far fields. First we examine the effect of the exponential term inside the integral in isolation. It produces a sinusoidal oscillation that is

fundamentally due to randomness of the event origin, manifested here by the term $\omega(x - x_0)/a$. A fast oscillation results in cancellation of the terms in the integrand and leads to a very small amplitude of the correlation. A slow oscillation results in a finite correlation. The oscillation is theoretically eliminated, and the correlation achieves its maximum amplitude, when

$$\cos\theta \;=\; \frac{1}{M_c(x_0)} \tag{37}$$

which defines approximately the direction of peak emission in supersonic jets. Because M_c changes with x_0, there is no single observer angle θ that will yield exact elimination of the oscillation. For jets with an initially supersonic convective Mach number the elimination condition can be satisfied exactly as long as x_0 stays within the potential core region, where M_c = constant. The elimination condition is expected to hold approximately at the aggregate angle of peak emission discussed in the context of Eq. 35 above. For subsonic jets, elimination is impossible but the frequency of the oscillation decreases as $\theta \to 0$; thus, we expect that the strongest correlation will be measured at angles close to the jet axis. As the polar angle departs significantly from the direction of peak emission, the correlation declines rapidly. At non-elimination conditions, the correlation declines with increasing frequency ω.

Of course, in Eq. 36 we have two contributors to polar directivity, the exponential term just discussed and the amplitude of $\widehat{W}$. The effect of the latter is largely filtered out by examining the coherence

$$C_{pP,\omega}(x,\theta) \;=\; \frac{|R_{pP,\omega}(x,\theta;\mathcal{R}/a)|^2}{R_{PP,\omega}(\theta)R_{pp,\omega}(x,0,0)} \tag{38}$$

or the normalized correlation

$$C_{pP}(x,\theta) \;=\; \frac{R_{pP}(x,\theta)}{\sqrt{R_{PP}(\theta)R_{pp}(x,0,0)}} \tag{39}$$

V. Initial Results

The results presented are based on a preliminary parameter optimization that seeks to match the far-field spectral density of a cold Mach 0.9 jet.[22] The optimization method is similar to that used in Ref. 10, namely the least-squares minimization of the difference between the modeled and measured spectral density in the far field. The optimization method is described briefly, followed by results of key statistical quantities.

A. Optimization

We consider a cold Mach 0.9 jet with radiator-surface growth rate $dr/dx = 0.08$, reflecting the recent experimental evaluation of this surface.[18] The acoustic Mach number U_j/a equals 0.84. The wavepacket envelope of Eq. 33 assumes the specific form

$$W(\eta) \;=\; \tanh\left(b_1\eta\right)^{\beta_1} \;\left[1 - \tanh\left(b_2\eta\right)^{\beta_2}\right] \tag{40}$$

This formulation allows fairly independent adjustments of the growth and decay of the wavepacket envelope, controlled by the first and second tanh terms.[10,22]

For given PDFs $f_{x_0}(\omega)$ and $f_n(\omega)$, the model predictions depend on the parameter vector

$$\mathbf{V} \;=\; \left(\frac{U_c(0)}{U_j}, b_1, b_2, \beta_1, \beta_2\right) \tag{41}$$

which describes the wavepacket convective speed and shape. Denoting the far-field sound pressure level as

$$\mathrm{SPL}(\mathcal{R},\theta,\omega) = 10\log_{10}\left[R_{PP,\omega}(\mathcal{R},\theta)\right]$$

we define the "normalized" SPL as

$$\overline{\mathrm{SPL}}(\theta,\omega) = \mathrm{SPL}(\mathcal{R},\theta,\omega) - \mathrm{SPL}_{max}(\mathcal{R},\omega)$$

where *max* denotes the peak value of the polar distribution. $\overline{\mathrm{SPL}}$ is independent of distance and describes the shape of the spectrum versus frequency and polar angle. Next, the modeled and experimental normalized

spectra are compared at discrete values of frequency $\omega_i, i = 1, \ldots, N_i$ and polar angle $\theta_j, j = 1, \ldots N_j$. We construct the cost function

$$F(\mathbf{V}) \;=\; \sqrt{\frac{1}{N_i N_j}\sum_{i=1}^{N_i}\sum_{j=1}^{N_j}\left[\overline{\mathrm{SPL}}_{mod}(\mathbf{V},\theta_j,\omega_i) - \overline{\mathrm{SPL}}_{exp}(\theta_j,\omega_i)\right]^2} \;+\; \sum_{l=1}^{N_l} Y_l(V_l) \tag{42}$$

The subscripts *mod* and *exp* denote the modeled and experimental quantities; N_l is the length of the parameter vector; and Y_l are appropriately defined penalty functions that constrain the parameters within reasonable ranges. The square root term represents the "standard error" of the modeled SPL. The parameter vector $\mathbf{V}$ was determined by minimizing the cost function, using the restarted conjugate gradient method of Ref. 23 (ACM TOM Algorithm 500). The process used N_i=25 frequencies spaced at equal logarithmic intervals, and $N_j = 10$ polar angles between 20° and 110° relative to the downstream axis. The scheme converged after about 50 function calls to an error around 1.5 dB and zero penalty function.

In the evaluation of the cost function, the amplitude $E(\omega)$ in Eq. 35 is irrelevant because the cost function is formulated in terms of normalized spectral densities. So, it can be set to unity for convenience. Once the minimization is completed, the modeled spectral density is reconstructed as follows:

$$\mathrm{SPL}_{mod}(\mathcal{R}_{exp},\theta,\omega) \;=\; \overline{\mathrm{SPL}}_{mod}(\theta,\omega) \;+\; \mathrm{SPL}_{exp,max}(\mathcal{R}_{\mathrm{exp}},\omega) - \mathrm{SPL}_{mod,max}(\mathcal{R},\omega) \tag{43}$$

With this last step, $E(\omega)$ is determined empirically.

The minimization process described by Eq. 42 was performed at fixed values of the parameters that define the PDFs for x_0 and n (μ and σ in Eq. 2; the constants involved in Eq. 16). These values were adjusted "manually", through a trial-and-error process, to achieve the best convergence while maintaining physically realistic ranges. The resulting values are $\mu = 3.4$, $\sigma = 0.9$, and the numerical constants involved in Eq. 16. Table 1 summarizes the result of the optimization. The PDF for x_0 is plotted in Fig. 3.

Table 1 Optimal parameters

$U_c(0)/U_j =$	0.620
$b_1 =$	0.987
$b_2 =$	0.564
$\beta_1 =$	1.852
$\beta_2 =$	2.984
$\mu =$	3.400
$\sigma =$	0.900

The resulting shape of the wavepacket is depicted in Fig. 7. Having determined all the parameters that impact the evaluation of the pressure fields, we are now in position to apply the relations of Section IV to evaluate the statistical quantities of interest.

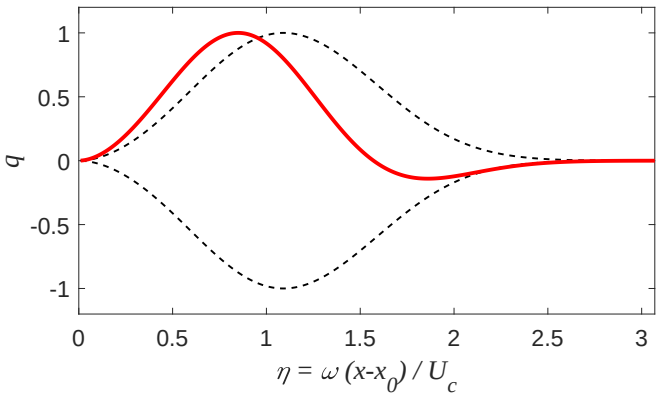

Figure 7. Real part (red line) and envelope (dashed line) of optimized wavepacket event (Eq. 33).

B. Far-field Autospectral Density

The far-field autospectral density is given by Eq. 35 and is presented here in terms of the sound pressure level

$$\mathrm{SPL}(\omega,\theta) \;=\; 10\;\log_{10} R_{PP,\omega}(\theta)$$

where normalization constants are omitted. Figure 8 compares the experimental and modeled distributions of SPL versus polar angle and Strouhal number. The modeled spectrum is in overall agreement with the experimental spectrum, except at high frequency and large polar angle where the modeled spectrum decays rapidly. The standard error, as defined by the first term on the right-hand side of Eq. 42, is 1.5 dB. It is notable that a single source produces a spectral density that broadens with increasing polar angle and matches, in an overall sense, the experimental spectral density. Although refinements are needed, Figure 8 indicates that the stochastic wavepacket model of Section IV has the potential to act as a basic noise source whose acoustic far field reproduces that of the actual turbulent jet.

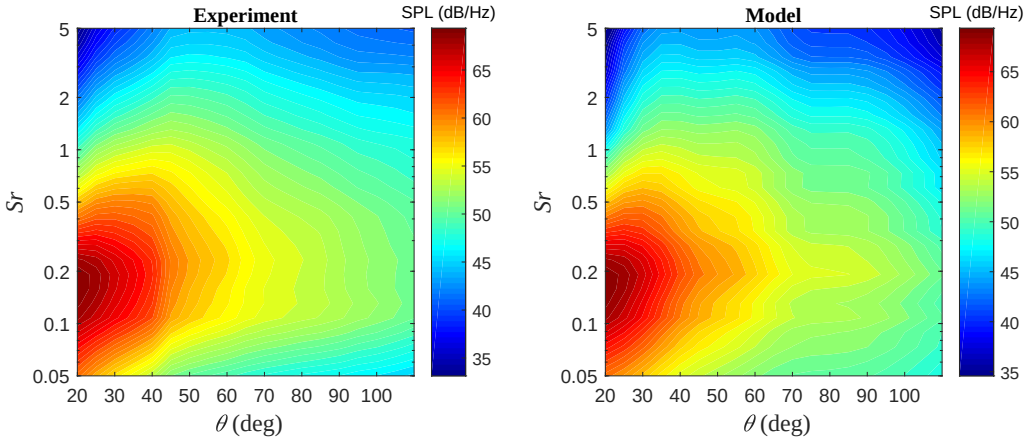

Figure 8. Experimental (left) and modeled (right) distributions of sound pressure level (decibel scale) versus polar angle and Strouhal number for Mach 0.9 cold jet.

C. Space-Time Correlation on Surface

The space-time correlation on the radiator surface is determined by combining Eqs. 24 and 33. It is presented here in normalized form, divided by the variance. The probe position is at $x/D_j = 4$, near the end of the potential core. As seen in Fig. 9, the shape of the space-time correlation captures the well-established experimental trends.[18,24,25] This is an encouraging indication that the stochastic event considered here contains the essential physics to be used as a fundamental model for the jet noise source.

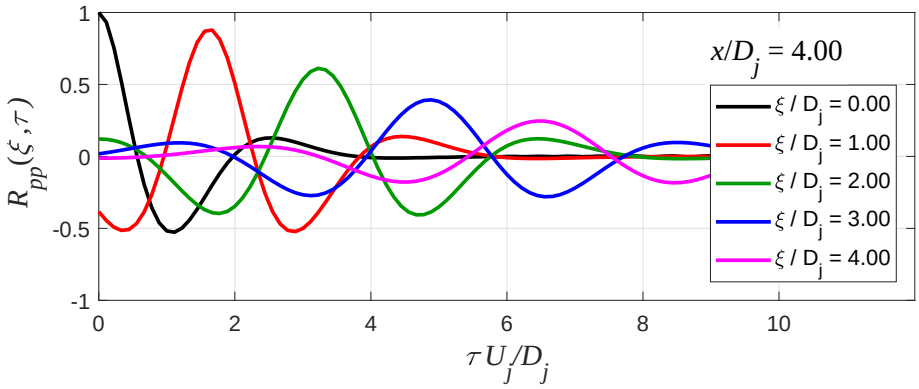

Figure 9. Space-time correlation on radiator surface at $x/D_j = 4$.

D. Surface to Far-Field Correlation

We examine the surface to far-field coherence given by Eq. 38. The surface probe is again located at $x/D_j = 4$. Figure 10 plots the coherence versus polar angle for various Strouhal numbers. The rapid decline with increasing polar angle is noted. Since the effect of the declining radiation efficiency with polar angle is accounted for by the normalization in the coherence, the trends in Fig. 10 are due primarily to the oscillatory term discussed in conjunction with Eq. 36. In other words, the decline in coherence is due to the random nature of the event origin x_0. At Strouhal number $Sr = 0.2$, the coherence declines by factor of ~ 30 as the polar angle increases from $\theta = 20°$ to $\theta = 90°$. At higher Strouhal numbers, the decline is even more pronounced.

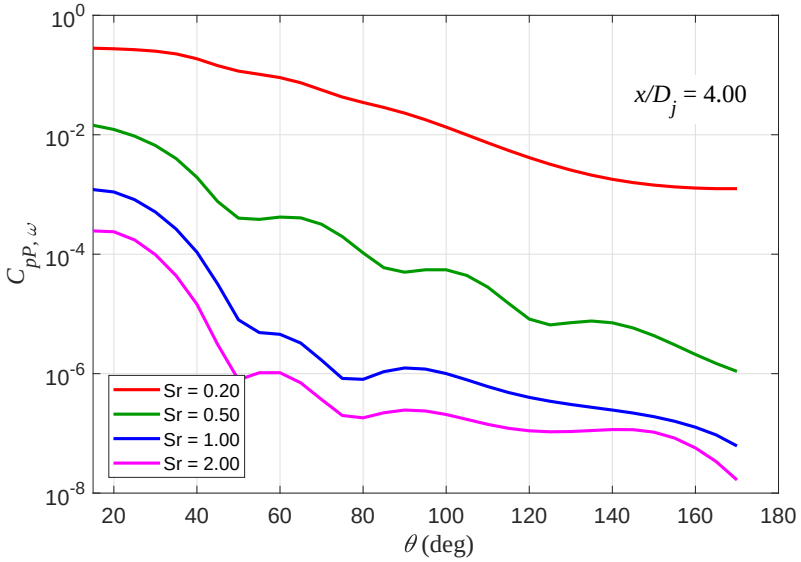

Figure 10. Surface to far-field coherence with probe at $x/D_j = 4$.

The integrated effect of the plots in Fig. 10 is captured by the overall correlation versus polar angle, plotted in normalized form (Eq. 39) in Fig. 11. Since this jet is subsonic, the correlation does not exhibit a maximum but keeps increasing with decreasing polar angle. The correlation value is 0.09 at $\theta = 20°$ and declines to 0.007 at $\theta = 90°$. Again, this decline is due primarily to the randomness of the event origin.

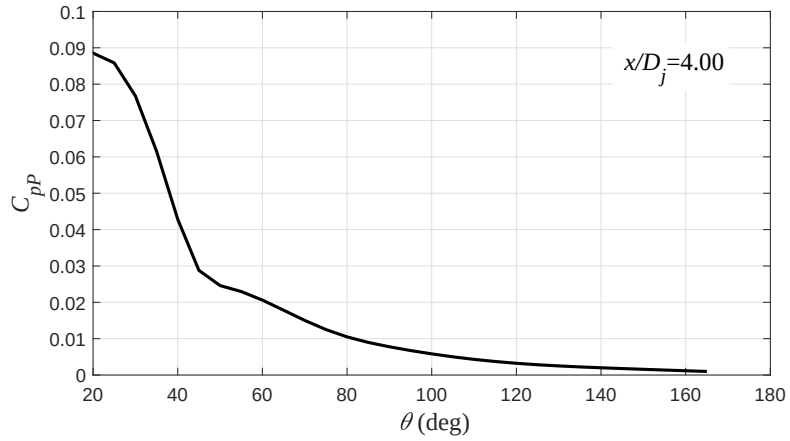

Figure 11. Normalized surface to far-field correlation with probe at $x/D_j = 4$.

The qualitative trends seen in Figs. 10 and 11 are consistent with experimental measurements of the correlation between density fluctuations in the jet and far-field sound emission (Ref. 11 and works cited therein), as well as experimental correlations of the near and far acoustics fields.[12] The present model indicates that the reduction in this correlation with increasing polar angle is not inconsistent with the coherent-structure model of the jet noise source.

VI. Concluding Remarks

We presented the development of a simple stochastic model for the noise source of a round turbulent jet, inspired by the statistics of coherent structures in shear layers as quantified by Bernal.[14] The model is defined on a surface at the rotational/irrotational boundary of the jet and comprises a linear pressure event (partial field) with random origin and random helical mode. The probability density function for the event's axial origin is derived from the statistics of coherent structures in shear layers, while the distribution for the helical mode is mostly empirical and driven by the need to match the polar directivity of far-field sound emission. The generic shape of the event is a self-similar wavepacket; the shape parameters were determined by least-squares matching of the far-field sound pressure level at a wide range of frequencies and polar angles. Initial results indicate that the model reproduces, in a qualitative sense, key statistics of the jet acoustic field, including the near-field space-time correlation, the broadening of the far-field spectral density with polar angle, and the coherence between the near and far fields. For the latter, the model indicates that the rapid decline in the coherence with increasing polar angle is primarily due to the randomness of the event's axial origin.

The potential value for this model lies not only in the development of predictive models for the jet noise itself but, most importantly, in the efficient prediction of the interaction of jet noise with nearby boundaries. The partial-field nature of the model, and the simplicity of the underlying basis function (Eq. 33, Fig. 7), makes it amenable to approaches like the boundary element method that can solve the propagation of a large number of partial fields at relatively low cost.[26,27] Recent experiments on the very near pressure field of dual-stream jets[18] provide guidance on the extension of this type of model to the emission from multi-stream jets.

A series of refinements, and a number of open questions, remain. The present model assumed full azimuthal coherence, whereas in reality the azimuthal coherence drops rapidly with increasing Strouhal number.[18] This means that, in future implementations, the event will have an envelope not only in the axial direction but also in the circumferential direction. In applying shear-layer statistics in the vicinity of the potential core, the issue of the jet "preferred mode" may need to be examined.[15,28] For the region past the potential core the flow cannot be characterized as a shear layer; new information on the large-scale turbulent statistics in that region is needed. Further, there are additional metrics that the model needs to be evaluated on, including the effect of source coherence on the sound radiation.[9,29]

References

[1]Ho, C., "Near Field Pressure Fluctuations in a Circular Jet," *NASA CR-179847*, Nov. 1985.

[2]Zaman, K., "Flow Field and Near and Far Sound Field of a Subsonic Jet," *Journal of Sound and Vibration*, Vol. 106, No. 1, 1986, pp. 1–16.

[3]Gudmundsson, K. and Colonius, T., "Instability Wave Models for the Near-Field Fluctuations of Turbulent Jets," *Journal of Fluid Mechanics*, Vol. 689, 2011, pp. 97–128.

[4]Morris, P., "A Note on Noise Generation by Large Scale Turbulent Structures in Subsonic and Supersonic Jets," *International Journal of Aeroacoustics*, Vol. 8, No. 4, 2009, pp. 301–316.

[5]Reba, R., Narayanan, S., and Colonius, T., "Wave-Packet Models for Large-Scale Mixing Noise," *International Journal of Aeroacoustics*, Vol. 9, 2010, pp. 533–558.

[6]Cavalieri, A., Jordan, P., Agarwal, A., and Gervais, Y., "Jittering Wave-Packet Models for Subsonic Jet Noise," *Journal of Sound and Vibration*, Vol. 330, May 2011, pp. 4474–4492.

[7]Jordan, P. and Colonius, T., "Wave Packets and Turbulent Jet Noise," *Annual Review of Fluid Mechanics*, Vol. 45, 2013, pp. 173–195.

[8]Cavalieri, A., Rodriguez, D., Jordan, P., and Colonius, T., "Wavepackets in the Velocity Field of Turbulent Jets," *Journal of Fluid Mechanics*, Vol. 730, Sept. 2013, pp. 559–592.

[9]Cavalieri, A. and Agarwal, A., "Coherence Decay and its Impact on Sound Radiation by Wavepackets," *Journal of Fluid Mechanics*, Vol. 748, April 2014, pp. 399–415.

[10]Papamoschou, D., "Wavepacket Modeling of the Jet Noise Source," *International Journal of Aeroacoustics*, to appear, 2018 (see also AIAA-2011-2835).

[11]Tam, C., Viswanathan, K., Ahuja, K., and Panda, J., "The Sources of Jet Noise: Experimental Evidence," *Journal of Fluid Mechanics*, Vol. 615, 2008, pp. 253–292.

[12]Crawley, M., Alkandry, H., Sinha, A., and Samimy, M., "Correlation of Irrotational Near-field Pressure and Far-field Acoustic in Forced High-Speed Jets," *AIAA Paper 2013-2188*, May 2013.

[13]Brown, G. and Roshko, A., "On Density Effects and Large Structure in Turbulent Mixing Layers," *Journal of Fluid Mechanics*, Vol. 64, 1974, pp. 775–816.

[14]Bernal, L., "The Statistics of the Organized Vortical Structure in Turbulent Mixing Layers," *Physics of Fluids*, Vol. 31, No. 9, 1988, pp. 2533–2543.

[15]Petersen, R. and Samet, M., "On the Preferred Mode of Jet Instability," *Journal of Fluid Mechanics*, Vol. 194, 1988, pp. 153–173.

[16]Papoulis, A., "Probability, Random Variables, and Stochastic Processes," McGraw-Hill, New York, 1965, pp. 125–127, 339.

[17]Papamoschou, D. and Rostamimonjezi, S., "Effect of Velocity Ratio on Noise Source Distribution of Coaxial Jets," *AIAA Journal*, Vol. 48, No. 7, 2010, pp. 1504–1512.

[18]Papamoschou, D. and Phong, V., "The Very Near Pressure Field of Single- and Multi-Stream Jets," *AIAA Paper 2017-0230*, Jan. 2017.

[19]Michalke, A. and Fuchs, H., "On Turbulence and Noise of an Axisymetric Shear Flow," *Journal of Fluid Mechanics*, Vol. 70, No. 1, 1975, pp. 179–205.

[20]McLaughlin, D., Morrison, G., and Troutt, R., "Experiments on the Instability Waves in a Supersonic Jet and their Acoustic Radiation," *Journal of Fluid Mechanics*, Vol. 69, 1975, pp. 73–95.

[21]Tam, C. and Burton, D., "Sound Generation by the Instability Waves of Supersonic Flows. Part 2. Axisymmetric Jets," *Journal of Fluid Mechanics*, Vol. 138, 1984, pp. 273–295.

[22]Papamoschou, D., "Prediction of Jet Noise Shielding," *AIAA Paper 2010-0653*, June 2010.

[23]Shanno, D. F. and Phua, K. H., "Minimization of Unconstrained Multivariate Functions," *ACM Transactions on Mathematical Software*, Vol. 6, No. 4, 1976, pp. 618–622.

[24]Doty, M. and McLaughlin, D., "Space-Time Correlation Measurement of High-Speed Axisymmetric Jets Using Optical Deflectometry," *Experiments in Fluids*, Vol. 28, March 2005, pp. 415–425.

[25]Morris, P. and Zaman, K., "Velocity Measurements in Jets with Application to Jet Noise," *Journal of Sound and Vibration*, Vol. 329, 2010, pp. 394–414.

[26]Chagrin, M. and Hideaki, I., "Minimization of Radiated Noise Using CDH/OPT/VAO," *SAE Paper 2005-01-2357*, May 2015.

[27]Cao, L., Wen, L., Xiao, J., and Liu, Y., "A Fast Directional BEM for Large-Scale Acoustic Problems based on the BurtonMiller Formulation," *Engineering Analysis with Boundary Elements*, Vol. 50, 2015, pp. 47–58.

[28]Kuo, C.-W., Cluts, J., and Samimy, M., "Effects of Excitation around Jet Preferred Mode Strouhal Number in High-Speed Jets," *Experiments in Fluids*, Vol. 58:35, 2017, pp. 1–15. DOI/10.1007/s00348–017–2329–7.

[29]Baqui, Y., Agarwal, A., Cavalieri, A., and Sinayoko, S., "A Coherence-Matched Linear Source Mechanism for Subsonic Jet Noise," *Journal of Fluid Mechanics*, Vol. 776, June 2015, pp. 235–267.